JOURNAL OF SPACECRAFT AND ROCKETS
Vol. 47, No. 6, November–December 2010

Intensified Low-Resolution Optical Spectroscopy of the Stardust Sample Return Capsule Entry

Peter Jenniskens*
SETI Institute, Mountain View, California 94043
and
Mike Koop and Jim Albers
Lockheed Martin Corporation, Sunnyvale, California 94045

DOI: 10.2514/1.40250

The radiation emitted by the Stardust sample return capsule during reentry into Earth's atmosphere on 15 January 2006 was measured with a staring airborne intensified camera, equipped with an objective transmission grating. The instrumental setup was designed to provide low-resolution spectra of the capsule's radiation, even if other instruments would fail in tracking the object. Spectra were recorded at the video frame rate of 30 Hz. The spectra covered the range of 380–860 nm, with a dispersion of 2.3 nm/pixel and a full-width-at-half-maximum resolution of 7 nm. Fully calibrated results, to an absolute precision of ∼17%, are presented for the time period from 09:57:17 to 09:57:43 Coordinated Universal Time, averaged over periods of 1 s. The data provided records of the CN band intensity detected throughout flight (unsaturated), the continuum emission (partially saturated), and the shock plasma emissions of oxygen and nitrogen during peak heating (partially saturated). A spectrum of wake radiation is also presented.

I. Introduction

SPECTROSCOPIC analysis of radiation was a key objective of the Stardust Sample Return Capsule (SRC) Entry Observing Campaign, which was executed with NASA's DC-8 airborne laboratory on 15 January 2006 [1,2]. A range of spectrographic cameras were deployed to measure the fireball's radiant energy. Here, we present results from an instrument called the intensified imaging spectrograph (INT1), which consisted of two staring intensified cameras with a wide $30 \times 40^\circ$ field of view. Redundancy of instruments was a key design feature to help address the wide range of brightness, diversity of spectral features, potential calibration uncertainties, and the difficulties of pointing and manual tracking. The INT1 cameras were meant to record both images (zero order) and low-resolution first-order spectra, in case none of the pointing instruments could locate the capsule in the sky. The field of view was chosen to ensure complete coverage, from initial rapid brightening until peak deceleration. Each camera was equipped with a transmission grating, placed in front of the lens, so that a simultaneous 380–860 nm first-order spectrum was recorded when the capsule became bright enough to saturate the zero-order image. Instrumental blooming also extended the potentially useful dynamic range of the measurements. As a result, flux measurements were possible when the capsule had a stellar magnitude ranging from about +6 to −10.

The forward-looking camera of INT1 recorded spectra from 09:57:17 to 09:57:47 Coordinated Universal Time (UTC), covering both the period of peak heating and peak deceleration. Here, we analyze these data to derive a series of fully calibrated spectra, intended for studies of surface heating, shock radiation, and radiation from ablation products of PICA: the phenol-impregnated carbon ablator material used as thermal protection. The physical conditions derived from these observations during entry, in combination with the postflight measured loss of the PICA, can be used to validate ablation models for PICA [3]. Indeed, the Stardust SRC entry was a system field test of PICA, a potentially important material for thermal protection systems of NASA's future spacecraft.

II. Instrument

The INT1 instrument (Fig. 1) consisted of two identical cameras: each equipped with an image intensifier, an objective lens, and an objective transmission grating. The image intensifier was a second-generation XX1332 tube, manufactured by Philips (now Photonis), which had a resolution of 18 line/mm and large 50 mm input and 40 mm output windows.

A Nikon 50 mm F1.8 Nikkor objective lens was stopped down to F2.8 and placed in front of the intensifier. Each camera was equipped with a 52-mm-diam, 600 line/mm transmission grating from Diffraction Products, Inc. (3090). The grating substrate was 1-cm-thick BK7 glass. The grating was blazed at 500 ± 50 nm (28°41' blaze angle). These are ruled gratings. The first-order Rowland ghost intensity was given by the factory as approximately 0.002%. The cameras were placed behind a Pyrex window with MgF_2 coating (labeled S/N 84 by the DC-8 aircraft operators) at port 570 on the left-hand side of the aircraft (Fig. 1).

The gain of the intensifier is controlled by the voltage across its multichannel plate, which accelerates and multiplies the electrons leaving the photocathode. The factory-provided gain-control characteristics [4] show that the intensifier response is linear up to a homogeneous photocathode illuminance of 1.4×10^{-4} lx, after which the ratio of phosphor screen luminance (L, in cd/m^2) to photocathode illuminance (E, in illuminance) changes according to

$$E/L = 6.7 \times 10^{-5} + 2.2 \times 10^{-7} * \exp(1.5 * L) \qquad (1)$$

The intensifier's output phosphor screen was imaged with a Sony HDV 1080i Handycam HDR-HC1 camcorder. The data were recorded at an 8-bit dynamic range, in digital form, at a rate of 29.97 frame/s, on a standard MiniDV cassette at high-definition 1920×1080 pixel 1080i resolution, with no calibrated time stamp but at the same time in analog form in National Television System Committee format, on a Sony TRV-65 Hi-8 camcorder at standard definition resolution, with a Global-Positioning-System-derived time stamp. These data were used for further analysis. The time

Presented at the 46th Aerospace Sciences and Exhibit, Reno, NV, 7–10 January 2008; received 5 August 2008; revision received 3 May 2010; accepted for publication 3 May 2010.

*Research Scientist, Carl Sagan Center, 515 North Whisman Road; Petrus.M.Jenniskens@nasa.gov. Member AIAA.

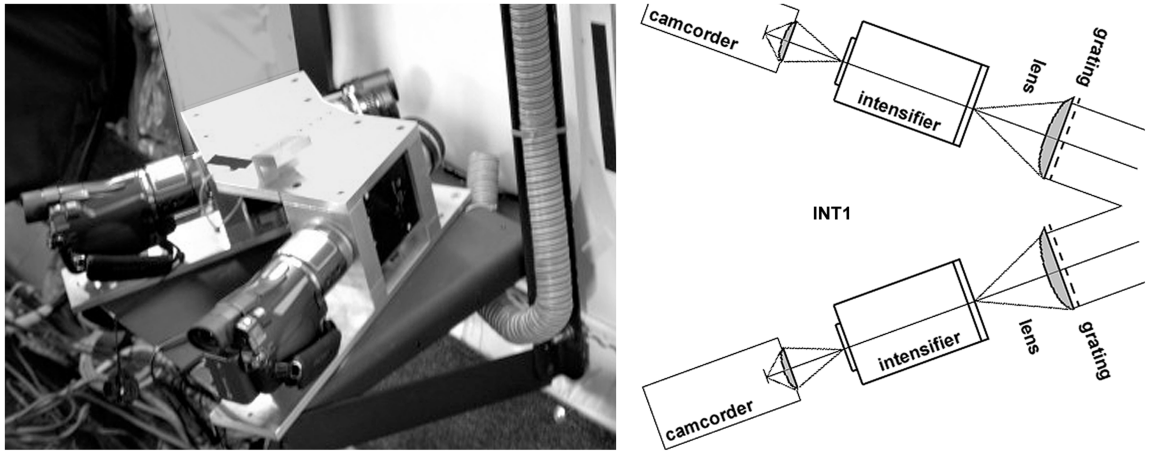

Fig. 1 The INT1 instrument consisted of two identical intensified cameras equipped with an objective grating.

signal (accuracy ± 0.001 s) was inserted through a video time inserter unit. The time was obtained from an aircraft-provided interrange instrumentation group time code "B" (IRIG-B) signal.

III. Methods of Data Calibration

Example images are shown in Figs. 2 and 3. The images were recorded to video. The video was digitized as 720×480 pixel array images at an 8-bit dynamic range, with pixel brightness units from 0–255 analog-to-digital units (ADU). The images are a combination of spectra and background light, including scattered light from inside the aircraft cabin. The sum of the first-order spectra and background-covered pixel brightness values were up to 235 ADU. The mean background value did not change significantly during the observation sequence.

A background image was subtracted to remove sky background light and scattered light from inside the aircraft cabin. The spectrum was extracted from the images by averaging a 10-pixel-wide band centered on each spectrum, providing sum pixel intensity in ADU per pixel column. Thirty spectra in intervals of 1 s were aligned by wavelength, using spectral features. The wavelength was calibrated by using the identified emission lines present in the Stardust SRC spectra itself. The pixel brightness was calibrated from the brightness of the stars observed in the same images. The brightness calibration translated the observed pixel brightness values in ADU to a flux density in $W/m^2/nm$, which involved a correction for instrument responsivity (including transmission of the aircraft window), with smaller corrections for vignetting, atmospheric extinction, and the geometric dilution from illuminating the lens at an angle.

The capsule moved through the field of view, from left to right. Figure 2 shows the capsule and wake (left), as well as the first-order spectrum. The zero-order image for 09:57:17 UTC is not in the field of view. The intensifier tube created a pincushion effect in the optical path, which caused the spectrum to gradually curve upward in later spectra (Fig. 2).

Until 09:57:43 UTC, the spectra appeared nearly linear, and the dispersion was independent of wavelength, within measurement error. Each 1 s averaged spectrum was independently wavelength-calibrated, using the known wavelength position of lines and bands. Emission lines were identified from other data sets [5]. In particular, we recognized lines of oxygen at 777.5 and 844.8 nm, nitrogen at 744.9 and 821.6 nm, strong bands of CN at 386.0 and 415.7 nm, as well as lines of zinc around 480 nm and potassium at 768.4 nm in early spectra.

The dispersion was found to gradually increase from 2.24 to 2.33 nm/pixel over the time period from 09:57:17 to 09:57:43 UTC. The measured line width is about full-width at half-maximum of 7 nm.

The air plasma emissions of oxygen and nitrogen were no longer recognized in the spectra past 09:57:40 UTC, which made wavelength calibration and the alignment of spectra problematic. Past 09:57:43 UTC, the spectra also became more severely affected by the vignetting, responsible for a brightness dropoff toward the edge of field of view. Hence, we do not consider observations past this time here. The spectra gradually moved out of the field of view after 09:57:57 UTC (Fig. 2).

The brightness calibration first involved subtracting sources of light unrelated to the capsule's entry. A dark curtain protected the window from in-cabin light, but it did not fully prevent light entering from below. Figure 3 shows an average of 16 frames taken from 09:57:24.3 to 09:57:24.9 UTC, contrast-enhanced to bring out these reflections in the window. This reflection was (nearly) constant during the observation and was subtracted from the Stardust data by

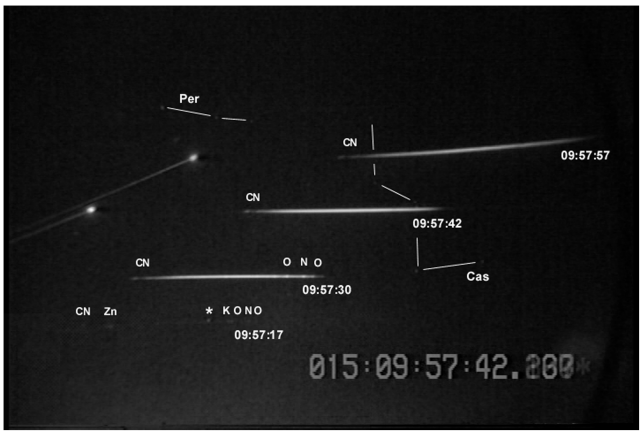

Fig. 2 Compilation of background-subtracted video frames of the forward-looking camera of INT1 at different times.

Fig. 3 Average of 16 frames taken at 09:57:24.3 to 09:57:24.3:24.9 UTC (contrast enhanced).

subtracting an average background image taken just before the capsule's entry. That did leave residues from background stars and star spectra, because the direction of the field of view had changed. In Fig. 3, stars from the constellations Perseus, Cassiopeia, and Andromeda are connected by lines. Few stars were detected, and only one caused a recognizable residue in the spectra.

Vignetting was caused by the lens and intensifier and was a function of distance away from the center of the lens-projected image on the intensifier. Figure 4 is a horizontal scan of brightness across the center of Fig. 3 and illustrates the effect of vignetting (dashed line) and stray light (excess values above the dashed line). Vignetting is normally recognized from how the intensity of the sky background falls off toward the edges of the field of view but, here, this functionality was only recognized away from the areas that contained background light. The generic function for vignetting is $\cos^4(\theta)$, with θ as the angle away from boresight, changing from 1.0 at the center of the field to 0.78 for viewing directions 20° away from the center direction (dashed line in Fig. 4).

The grating was illuminated at an angle. From 09:57:17 to 09:57:43 UTC, that angle changed from 33 to 16° aft. To account for this, we applied a geometric dilution factor, representing the dilution of flux when illuminating a surface at an angle, taken to be proportional to the cosine of this angle, where the brightness is corrected to normal incidence exposure. This factor changed from 0.84 to 0.96 and is accurately known.

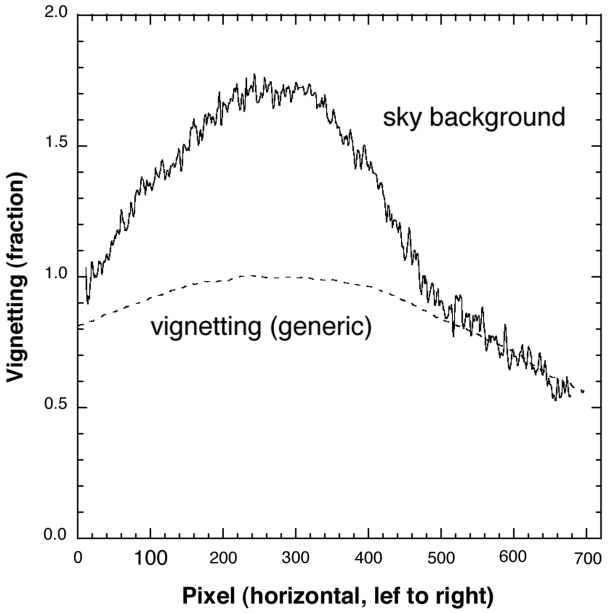

Fig. 4 Horizontal scan of pixel brightness across the center of Fig. 3.

The wavelength-dependent atmospheric extinction was calculated using the MODTRAN (moderate-resolution atmospheric transmission) radiation transfer algorithm [6]. The extinction is dominated by the ozone absorption in the line of sight from the aircraft to the capsule. Atmospheric extinction spectra were calculated for the known altitude of the aircraft and for a range of the capsule's altitude and elevation above the horizon. From 09:57:17 to 09:57:43 UTC, the capsule's elevation above the horizon changed from 7.7 to 17.4° (Fig. 2).

The transmission curve of the window for normal incidence and unpolarized light was measured in the laboratory. The transmission of the window dropped off gradually below 400 nm and was gray at higher wavelengths. The angle of the SRC relative to the boresight direction of the window changed from about 6° aft to 11° forward. The resulting small change in the window transmission (proportional to one over the cosine of this angle) was neglected.

The instrumental response, including the transmission of the window, is shown in Fig. 5a. The value of the response, in pixel brightness unit (ADU) per flux unit ($W/m^2/nm$), corresponds to the sum of pixel brightness integrated over a 10-pixel-long column perpendicular to the dispersion direction (after background subtraction and correction for vignetting) for a given pixel in the dispersion direction, which would be generated by an amount of flux falling onto the aircraft window.

Dots in Fig. 5a show the instrumental response derived by comparing the INT1 spectra (in ADU, after correction for geometric dilution, vignetting, window transmission, and atmospheric extinction) to the fully calibrated spectra observed by the echelle-based spectrograph for the crisp and high efficient detection of low light emission (ECHELLE) [5], observed in the period 09:57:19–22 UTC, when the INT1 spectra were weak and unsaturated. The smooth fit to the data in Fig. 5a (thick black line) was adopted to correct the data for responsivity before 09:57:23 UTC.

The measured responsivity is compared with the product of factory-provided responsivity and transmission data (shown on an arbitrary scale). The factory-provided intensifier quantum efficiency dropped off rapidly above 860 nm and below 380 nm. The transmission of the Nikon lens was measured in the laboratory and dropped off rapidly below 380 nm. The product of all contributions (including the window under normal incidence light) is shown as a thin line in Fig. 5a as marked product response (slightly displaced from the measured data for clarity). The measured response (dots with error bars in Fig. 5a) is somewhat less around 450 nm than the

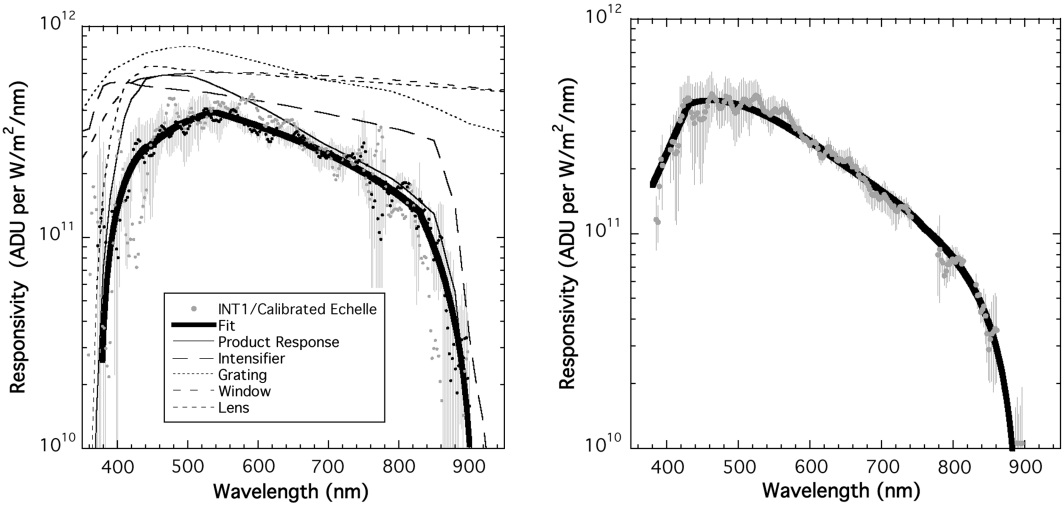

a) b)

Fig. 5 Spectral response curve of INT1 in first order. The graph on the right shows the effect of partial saturation in the period 09:57:23–25 UTC.

product response but, otherwise, there is good agreement. Such discrepancy can originate in the response of the grating, which was illuminated under different conditions than used to measure the factory-provided response curve.

In Fig. 5b, the same comparison was made with ECHELLE data from the period 09:57:23–25 UTC. Compared with Fig. 5a, INT1 is less responsive in the brighter part of the spectrum between 500 and 800 nm. This nonlinearity points to saturation, partially compensated by blooming in the image intensifier. To first approximation, we took saturation into account by adopting the responsivity of Fig. 5b for all spectra after 09:57:25 UTC.

An internal calibration of the absolute response was provided by the brightness of background stars. Broadband photometric data and spectral classifications for the stars were found in the SIMBAD astronomical data archive. The sum pixel brightness of 13 stars in Perseus, Cassiopeia, and Andromeda was measured from the same background-subtracted images used to derive the Stardust SRC spectra. This sum pixel intensity was compared with that calculated from each of the star spectra, as follows. The spectrum of each star was matched to the reported broadband photometric data in the B, V, R, and I Johnson photometric band system. That spectrum was then multiplied by the response curve of Fig. 5a and corrected for vignetting, window transmission, and atmospheric extinction. No geometric dilution factor was needed, because the incidence angle of the starlight was normal. After taking into account that the ratio of light distributed in first order, relative to zero order, is 1.37 ± 0.17, the observed sum pixel brightness for the zero order of each star image was found in good agreement with the calculated sum pixel brightness for the combined first-order spectrum (Fig. 6).

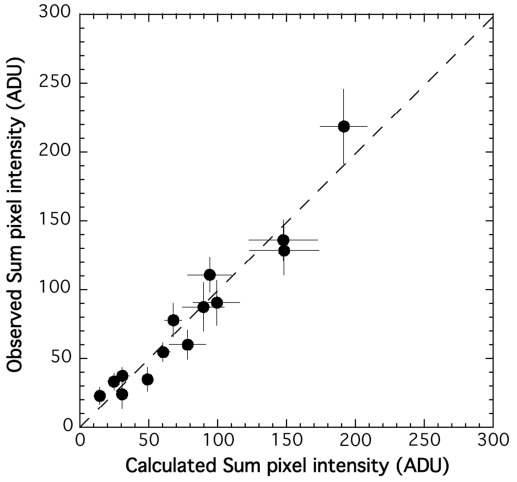

Fig. 6 Absolute calibration of responsivity from the brightness of background stars.

IV. Results

A. Capsule Reentry Spectrum

An overview of calibrated spectra is shown in Fig. 7. Each spectrum represents an average of 1 s of data, plotting flux density versus wavelength. These spectra are not, strictly speaking, the apparent flux just outside the aircraft window, since they are corrected for lost light due to atmospheric extinction between SRC and the observer.

Main emission features are marked. In early spectra, an asterisk (∗) marks an artifact due to emission from the background star Gamma Andromedae.

Figure 7 quantifies the abrupt fading of the air plasma emissions of oxygen and nitrogen around 09:57:37 UTC. The CN band continues to emit at near-constant intensity past peak heating, which occurred around 09:57:31 UTC (see next). At early times, zinc is also detected, a product of the ablation of a paint layer on the capsule [5].

B. Wake Spectrum

Just below the spectrum of the capsule was a faint spectrum of the capsule's wake. The period 09:57:42.3 to 09:57:42.9 UTC was selected for analysis, when the wake was bright and centered in the field of view. Over a distance corresponding to about 40 km (5 s of flight) along the trajectory behind the capsule, this emission was averaged and corrected for vignetting, extinction, and the instrumental response of Fig. 5a.

The wake emission (Fig. 8) has the spectral shape of a radiating blackbody with a temperature $T \sim 3300$ K, shown as a line fitted to the data in Fig. 8.

It is possible that this wake was caused by hot solid carbonaceous particles, recondensed or ablated from the capsule's heat shield. These particles were small enough to emit efficiently at visual and near-ultraviolet wavelengths. If so, they cooled little over the cause of 5 s, having a temperature not unlike that of the capsule's surface at that time.

V. Discussion

The continuum flux density gradually increased from 09:57:17.5 to 09:57:43.5 UTC, initially from the surface becoming hotter with time (until peak heating) and, later, from the capsule approaching the observer. As a result, the spectra became brighter and, on top of a background of sky emissions, became saturated in the brightest central parts where the instrumental response was highest.

To determine how well Fig. 5b compensates for this saturation, we compare the measured flux at wavelength 548 nm (•) with that measured by other instruments (Fig. 9). The wavelength of 548 nm

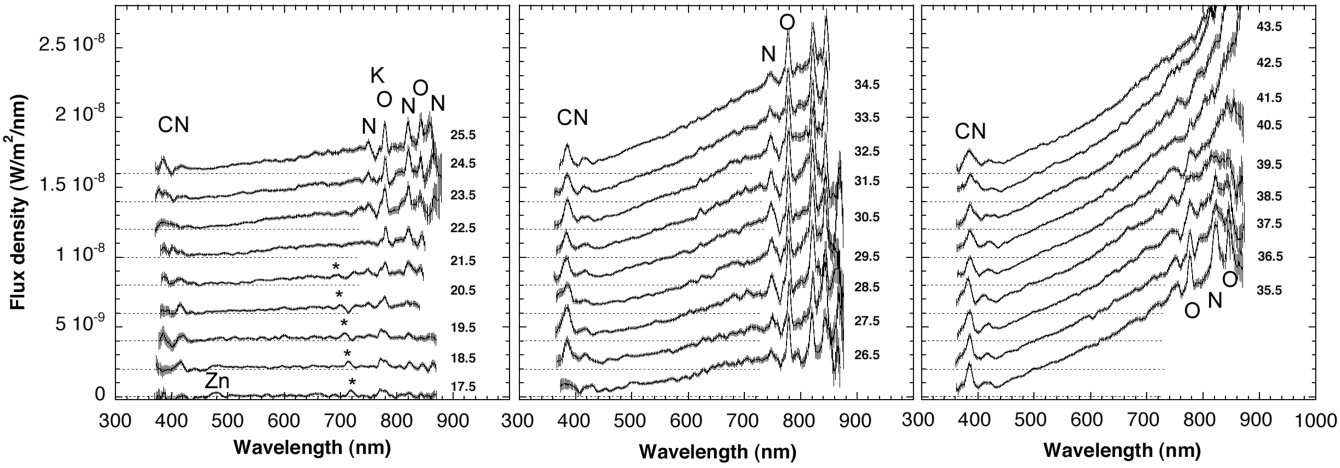

Fig. 7 Temporal evolution of calibrated INT1 spectra. For clarity, spectra are displaced by units of 1 × 10^{-9} W/m²/nm, the baseline of each spectrum given by a dashed line. Time is given in seconds after 09:57:00 UTC.

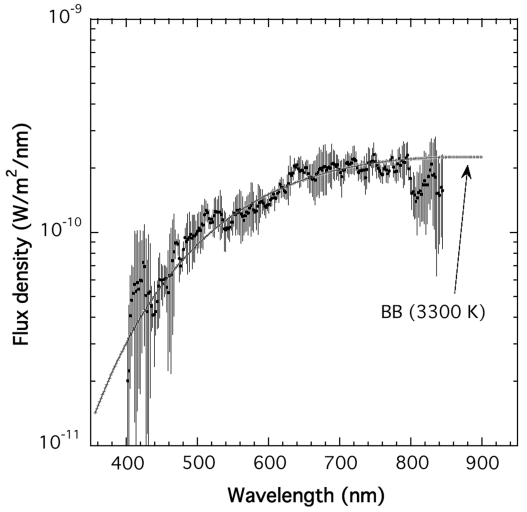

Fig. 8 Wake spectrum at 09 : 42.6 ± 0.3 UT. A blackbody curve for $T = 3300$ K was aligned with the observed spectrum.

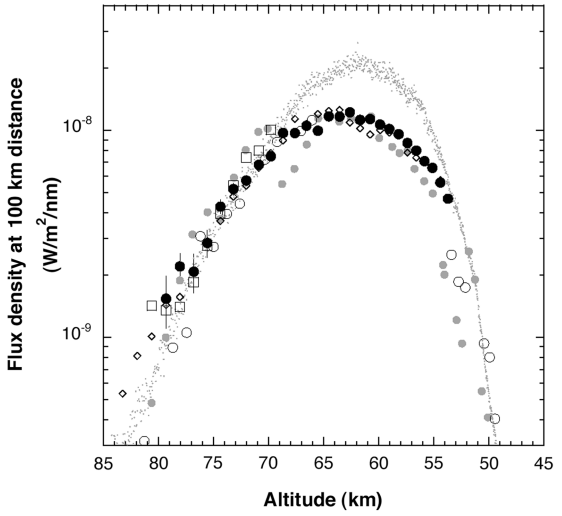

Fig. 9 The temporal variation of the 548 nm flux detected from the SRC from a distance of 100 km with atmospheric extinction removed.

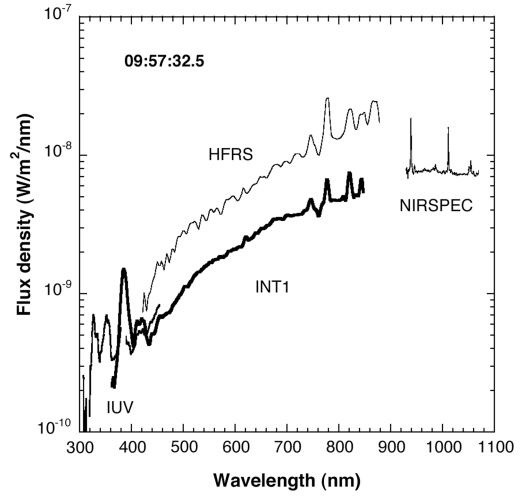

Fig. 10 Apparent flux density at the time of peak heating. Results for INT1 (this work) are compared with those of IUV [10], HFRS [7], and NIRSPEC [9] instruments.

was arbitrarily chosen, being the center of the Johnson photometric V band. Error bars pertain to random measurement errors and do not include the systematic uncertainty in the absolute calibration (17%). All data were normalized to that seen at a distance of 100 km, based on the known distance to the capsule (flux being proportional to the inverse square of the distance between the SRC and the observer). The 100 km distance is an arbitrary value, commonly used in meteor astronomy. The benefit of this normalization is that the flux density values of Fig. 9 are now independent of distance and proportional to the intensity of 548 nm light emitted from the surface of the capsule at that altitude (with the caveat that these results are not corrected for the projected surface area of the capsule).

Leading up to peak heating, the INT1-derived 548 nm flux density data follow those derived from ECHELLE [5] (squares in Fig. 9), high-frame-rate spectrograph (HFRS) [7] (dots), digital imager (DIM) [8] (○), near-infrared spectrometer (NIRSPEC) [9] (gray dot), and intensified UV spectrometer (IUV) [10] (scaled, ◇).

Once the capsule penetrated below 70 km, INT1-derived 548 nm flux density values follow the NIRSPEC and IUV data [9], derived indirectly from 1008 and 450 nm flux measurements, respectively. After that, NIRSPEC data sometimes fall below the trend measured by INT1, only because some flux was lost due to deliberately induced motion blurring.

Both INT1 and NIRSPEC fall a factor of two below the trend measured by HFRS (Fig. 9). It is possible that both instruments suffered from a change in gain setting, but INT1 did not show the anticipated change in the background signal level if that was the case.

The INT1 spectra do appear suitably corrected. Figure 10 compares the fully calibrated 1 s averaged INT1 spectrum at the time of peak heating with those derived from the IUV [10], HFRS [7], and NIRSPEC [9] instruments. The INT1 spectrum at this time overlaps the minima in the IUV spectrum and aligns well with the near-infrared spectrum derived from NIRSPEC. The $\Theta = 0 - 0$ band of CN at 388 nm is saturated in the IUV data but not in INT1. In between the unsaturated parts below 400 nm and above 800 nm, Fig. 5b appears to provide a reasonable approximation of the instrument's responsivity.

VI. Conclusions

The INT1 instrument operated as expected and recorded suitable low-resolution spectra of the capsule's radiation over the period 09:57:17 to 09:57: 43 UTC. These low-resolution INT1 results add to those of other instruments, such as ECHELLE, that covered only part of the entry trajectory. A mostly successful effort was made to compensate for instrumental saturation, using the instrument's response at times when the ECHELLE instrument measured the spectrum independently. Behind the image of the capsule, a strong wake was observed, a spectrum of which was measured. The spectrum identified the source of the wake emission due to hot solid particles. Models that compare the observed spectra to model calculations of capsule-surface heating and PICA ablation are presented in a separate paper [3].

The observations of the Stardust SRC entry are expected to remain a unique system field test for a long time to come. The observational data and the calibration files will be archived for this purpose. The present paper serves to document the files in hand.

Acknowledgments

This work was funded and managed by the Orion Thermal Protection System Advanced Development Project and the NASA Engineering and Safety Center. We thank H. Su of the Airborne Science and Technology Laboratory at NASA Ames Research Center for the extinction calculations. NASA's DC-8 airborne laboratory was deployed by the University of North Dakota/National Suborbital Education and Research Center, under contract with NASA Wallops Flight Center. D. Jordan acted as the NASA program manager.

References

[1] Jenniskens, P., Wercinski, P., Olejniczak, J., Raiche, G., Kontinos, D., Allen, G., Desai, P. N., ReVelle, D., Hatton, J., Baker, R. L., Russell, R. W., Taylor, M., and Rietmeijer, F., "Preparing for Hyperseed MAC: An Observing Campaign to Monitor the Entry of the Genesis Sample Return Capsule," *Earth, Moon, and Planets*, Vol. 95, Nos. 1–4, 2004, pp. 339–360. doi:10.1007/s11038-005-9021-2

[2] Jenniskens, P., Kontinos, D., Jordan, D., Wright, M., Olejniczak, J., Raiche, G., Wercinski, P., Desai, P. N., Taylor, M. J., Stenbaek-Nielsen, H. C., McHarg, M. G., Abe, S., Rairden, R. I., Albers, J., Winter, M., Harms, F., Wolf, J., ReVelle, D. O., Gural, P., Dantowitz, R., Rietmeijer, F., Hladiuk, D., and Hildebrand, A. R., "Preparing for the Meteoric Return of Stardust," *Proceedings of the Workshop on Dust in Planetary Systems*, edited by A. Grapps, and E. Gruen, ESA, SP 643, 2007, pp. 7–10.

[3] Trumble, K. A., Cozmuta, I., Sepka, S., and Jenniskens, P., "Postflight Aerothermal Analysis of Stardust Sample Return Capsule," *Journal of Spacecraft and Rockets*, Vol. 47, No. 5, 2010, pp. 765–774. doi:10.2514/1.41514

[4] "Image Intensifier Tubes, Product Specification for the XX1330 Family," Photonis Imaging Sensors, Sturbridge, MA, 9 Jan. 1995.

[5] Jenniskens, P., "Observations of the Stardust Sample Return Capsule Entry with a Slitless Echelle Spectrograph," *Journal of Spacecraft and Rockets*, Vol. 47, No. 5, 2010, pp. 718–735. doi:10.2514/1.37518

[6] Berk, A., Anderson, G. P., Bernstein, L. S., Acharya, P. K., Dothe, H., Matthew, M. W., Adler-Goldern, S. M., Chetwynd, J. H., Richtmeier, S. C., Pukall, B., Allred, C. L., Jeong, L. S., and Hoke, M. L., "MODTRAN4 Radiative Transfer Modeling for Atmospheric Correction," *Proceedings of SPIE: The International Society for Optical Engineering*, Vol. 3756, Oct. 1999, pp. 348–353. doi:10.1117/12.366388

[7] McHarg, M. G., Stenbaek-Nielsen, H. C., Kanmae, T., and Jenniskens, P., "Observations of the Stardust Sample Return Capsule Entry Using a High Frame Rate Slit-Less Spectrograph," *Journal of Spacecraft and Rockets* (submitted for publication).

[8] Wercinski, P. F., and Jenniskens, P., "Digital Still Snapshots of the Stardust Sample Return Capsule Entry," *Journal of Spacecraft and Rockets*, Vol. 47, No. 6, 2010, pp. 889–894. doi:10.2514/1.40248

[9] Taylor, M. J., and Jenniskens, P., "Near-Infrared Spectroscopy of the Stardust Sample Return Capsule Entry: Detection of Carbon," *Journal of Spacecraft and Rockets*, Vol. 47, No. 6, 2010, pp. 878–883. doi:10.2514/1.38075

[10] Rairden, R. L., and Jenniskens, P., "Near-Ultraviolet Spectroscopy of the Stardust Sample Return Capsule Reentry," *Journal of Spacecraft and Rockets*, Vol. 47, No. 5, 2010, pp. 753–756. doi:10.2514/1.40440

D. Kontinos
Guest Editor